8328 *J. Phys. Chem. A* **2002,** *106,* 8328−8338

Beam Study of the Luminescent E−E Energy Transfer Reaction Kr($^3P_2$) + N_2 → Kr + N_2(B $^3\Pi_g$) at High Resolution and Variable Collision Energy†

R. Bachmann, R. Ehlich, Ch. Ottinger,* and T. Rox

Max-Planck-Institut für Strömungsforschung, Bunsenstrasse 10, 37073 Göttingen, Germany

N. Sadeghi

Laboratoire de Spectrométrie Physique, Université Joseph Fourier de Grenoble I and CNRS (UMR 5588),
B.P. 87, 38402 Saint-Martin-d' Hères Cedex, France

Received: December 31, 2001; In Final Form: May 2, 2002

Colliding a beam of metastable Kr atoms with an N_2 gas target, the resulting $N_2(B\ {}^3\Pi_g \rightarrow A\ {}^3\Sigma_u^+)$ emission was observed with a spectral resolution of up to 0.15 nm fwhm. Optical multichannel detection was employed, using a cooled diode array detector. This allowed the first rotationally well-resolved product emission spectra from the Kr* + N_2 reaction to be obtained. Also, the beam energy was varied between 69 and 191 meV$_{CM}$ by seeding with H_2. The rovibrational product distributions were derived from spectral simulations. In agreement with the literature, nonresonant (exothermic) E−E transfer was observed, populating the vibrational levels $N_2(B,v'=4-12)$. This broad distribution was found to be essentially independent of the collision energy. The product rotation could be well described by Boltzmann distributions with T_{rot} = 1300−1050 K for v' = 5−12 at low and 1750−1400 K at high collision energy. A discussion of the reaction mechanism is given in terms of two alternative models, involving either an intermediate ion pair formation or a direct covalent curve crossing. Comparisons are made with the related reactions of Ar and Xe metastables.

I. Introduction

Chemiluminescent reactions of metastable rare gas atoms have attracted great interest in the past, notably in connection with laser technology. In collisions with halogen molecules, exchange reactions lead to excited species, which are responsible for the excimer laser operation. Recognizing the alkali-like electronic structure of a metastable state such as Xe* (...5p^5 6s), the reaction Xe* + Cl_2 → XeCl* + Cl has been described by a harpooning mechanism, whereby an intermediate ion pair Xe^+ + Cl_2^- is formed.[1] Optical emission has also been observed in collisions of metastable rare gas atoms Ar*, Kr*, and Xe* with N_2 molecules, in this case as a result of electronic energy transfer. For example, N_2(C) emission originates from collisions of Ar*, Kr*, and Xe* with N_2,[2,3] while N_2(B) product emission has been reported from Kr* + N_2[4−7] and Xe* + N_2[8−10] impact. For convenient future reference, Figure 1 shows the potential energy curves of the relevant electronically excited states of N_2 together with the energy levels of metastable Ar, Kr, and Xe.

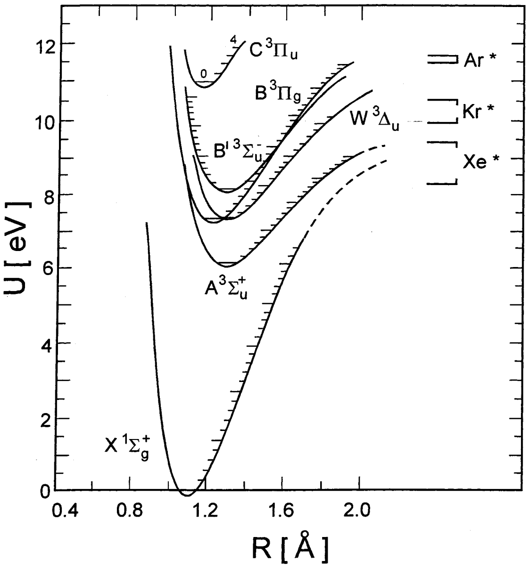

Figure 1. Potential energy curves of some electronic states of N_2 that are relevant to this work. The energy levels of metastable Ar, Kr, and Xe are indicated on the right, the upper (lower) bracket referring to the $^3P_0$ ($^3P_2$) state in each case. In this work, only the $^3P_2$ levels are relevant.

The much-studied energy transfer reaction

$$Ar(^3P_{0,2}) + N_2 \rightarrow Ar + N_2(C\ ^3\Pi_u) \qquad (1)$$

has been interpreted[3] to proceed via an initial harpooning step forming Ar^+ + N_2^-, analogous to the halogen case, although the electron affinity of the target is here negative. The vibrational distribution of the product $N_2(C,v')$, derived from spectral analysis of the subsequent N_2(C →B) emission, was found to be concentrated at v' = 0[3]. This preference for a vibrational exit channel with considerable exothermicity (0.517 eV) is consistent with the view of the strongly attractive (Coulombic) potential acting during the intermediate $Ar^+{-}N_2^-$ ion pair stage. Dominant population of strongly exothermic vibrational exit channels was also observed[4−7] in the reaction

$$Kr(^3P_2) + N_2 \rightarrow Kr + N_2(B\ ^3\Pi_g) \qquad (2)$$

---

† Part of the special issue "Donald Setser Festschrift".

* Corresponding author. Fax: +49 (551) 5176-607.

10.1021/jp0146723 CCC: $22.00

However, in the earlier of these studies,[4−6] done in flowing afterglow systems, the product vibrational distribution was degraded by collisional vibrational relaxation to a greater[4,5] or (using Ne carrier gas[6]) lesser extent. This problem was eliminated in a low-pressure beam/gas experiment,[7] where the true, nascent vibrational distribution of $N_2(B,v')$ could be measured. It is quite broad and peaks at $v' = 7$, corresponding to a reaction exothermicity of 1.156 eV. These results for Ar and Kr are in sharp contrast to the reaction

$$Xe(^3P_2) + N_2 \rightarrow Xe + N_2(B\ ^3\Pi_g) \qquad (3)$$

where the slightly *endo*thermic product vibrational channel $N_2(B,v'=5)$ ($\Delta E = 0.059$ eV) was found to be very selectively populated (see refs 6 and 8−10 and references therein). This could be explained by a potential model that involves crossings between purely covalent curves.[11] Crossings with the Coulombic ion pair potentials are here energetically inaccessible.

In the interpretation of the energy transfer mechanism, detailed observations of the rotational product excitation have generally proved very helpful. This is especially true of reaction 3, where the product formed in $v' = 5$ was found to be rotationally "cold" ($T_{rot} = 230-340$ K, for collision energies 56−270 meV_{CM}[9]), while the minor fraction in $v' \leq 4$ had $T_{rot} = 700-1200$ K.[11] Again, because of the possibility of collisional rotational relaxation during the rather long radiative lifetime ($\tau = 4-5\ \mu s$) of $N_2(B)$, a beam experiment is necessary to obtain this information. For reaction 1, high rotational excitation of the $N_2(C)$ product was also observed in crossed-beam, beam-gas, and afterglow experiments[2,12,13] (because of the short radiative lifetime of $N_2(C)$, $\tau = 40$ ns, the relaxation problem is here much less severe). Detailed measurements of the rotational distributions allowed conclusions to be drawn on the preferred collision geometry.[2]

For the Kr* + N_2 reaction, eq 2, rotationally resolved spectra have previously not been reported. The examples of reactions 1 and 3 have shown, however, that the information on the rotational product excitation can be the key to a detailed understanding of the reaction mechanism. In the present work we have therefore determined the rotational distributions in the vibrational levels $v' = 5-12$ of $N_2(B,v')$ formed in reaction 2, as well as the dependence of the rotational excitation on the collision energy. Experimentally this progress was possible by combining the intense metastable atom beam, developed in Göttingen, with a powerful optical multichannel detector system, made available by the University of Grenoble.

II. Experimental Section

The molecular beam apparatus was the same as that used in ref 9. In the present work, the discharge conditions for optimum generation of Kr* metastables were 4 A dc current at ∼120 V (seeded). The Kr stagnation pressure was 16 mbar. For moderate seeding, a Kr:H_2 ratio of 10:15 mbar was employed. In the high-resolution experiments stronger seeding was used, since this was found to increase the luminescence intensity. The Kr:H_2 pressure ratio was then 16:34 mbar. The N_2 target gas pressure, at room temperature, was 4×10^{-3} mbar. The diameter of the Kr* beam in the observation region was ∼10 mm. As in ref 9, the luminescence light was guided to a grating spectrometer by means of an optical fiber bundle. Its front end (2 × 20 mm, oriented parallel to the beam) was brought very close (∼8 mm) to the beam axis. Its acceptance angle is 70°. In comparison with the Xe experiments,[9] many of the experimental parameters (discharge current, nozzle and target gas pressure, beam diameter) were pushed almost to their limits, because the first exploratory measurements with a scanning monochromator[14] had shown that the $N_2(B)$ emission intensity is much smaller with Kr* than with Xe*. During the present work, a few comparative experiments were done with Xe* instead of Kr*, under otherwise similar conditions, and again the peak luminescence intensity with Kr* was found to be weaker than with Xe* by almost 2 orders of magnitude. Considering that in the broad Kr* + N_2 spectra the total luminescence intensity is spread over many bands (see below), while in the Xe* case it is concentrated almost entirely in the emission from $v' = 5$,[9] these qualitative observations are in good agreement with the published absolute luminescence rate constants, which are 0.2×10^{-11} cm^3/s for Kr* + N_2 and 1.7×10^{-11} cm^3/s for Xe* + N_2, respectively.[6]

The Kr* velocity was not directly measured in this work. Instead, it was inferred from the velocity of metastable Xe atoms produced from the same source, which had previously been measured by laser-induced fluorescence as well as by TOF measurements.[15] For the unseeded beam the mean lab-frame kinetic energy of Kr* is taken to be the same (110 meV) as for Xe*, because the velocity at full expansion, $v = (\gamma/\gamma - 1)^{1/2}(2kT/m)^{1/2}$ scales as $m^{-1/2}$ (assuming identical nozzle temperatures in the Xe and Kr experiments). For the 10:15 mbar Kr:H_2 seed ratio, the Kr* velocity was obtained by interpolating between the Xe* velocities measured for the Xe:H_2 pressure ratios 9:11 and 9:21 mbar.[15] The assumption is made here that the velocity slip between the light and the heavy jet species is similar for comparable Xe/H_2 and Kr/H_2 mixtures.[16] This yields a Kr* lab system kinetic energy of 260 meV. For the 16:34 mbar Kr:H_2 mixture, the Kr* velocity could again be estimated from the 9:21 mbar Xe:H_2 data given in ref 15. While these two pressure ratios are almost the same, the higher total stagnation pressure in the former case will increase the velocity over that measured for Xe[15] by almost 35%.[15,16] This results in a Kr* lab-frame energy of 646 meV. Transforming to the center-of-mass frame, one finds 39.5, 65.0, and 161.5 meV_{CM} for the unseeded, mildly seeded, and strongly seeded conditions, respectively. To these values the mean energy of the random N_2 motion, relative to a Kr atom (assumed stationary), has to be added[15] to obtain the correct average relative energy for the Kr beam/N_2 gas arrangement used here. The final results are $\langle E_{CM} \rangle = 69$ meV (unseeded), 94 meV (mildly seeded), and 191 meV (strongly seeded).

Either a low resolution $^1/_4$ m spectrometer (Jarrell-Ash, 1200 l/mm grating, blazed at 600 nm) or a high-resolution 0.6 m instrument (HRS, Jobin-Yvon, 1200 l/mm grating, blazed at 500 nm) were used. Both were operated in conjunction with a thermoelectrically cooled (∼25 °C) intensified diode array (OSMA, Spectroscopy Instruments, Inc., 700 pixels spaced at 25 μm center-to-center). With an entrance slit width of 100 μm, the spectral resolution was ∼0.45 nm fwhm with the Jarrell-Ash and 0.15 nm fwhm with the Jobin-Yvon instrument. Typical acquisition times were 10−20 min per spectrum. After subtraction of the dark current (∼4000 counts/min per diode, but reproducible to within ±5 cts/min), which was for each spectrum recorded for the same length of time as the spectrum itself, the accumulated signal was on the order of a few thousand counts/channel.

The optical multichannel detector was essential for the measurement of the very weak emission studied here. It enabled the data collection times to be reduced by a very large factor, compared to the conventional scanning monochromator/discriminator/multichannel scaler technique. Thus, in trial runs, spectra were taken of the afterglow of a metastable N_2* beam

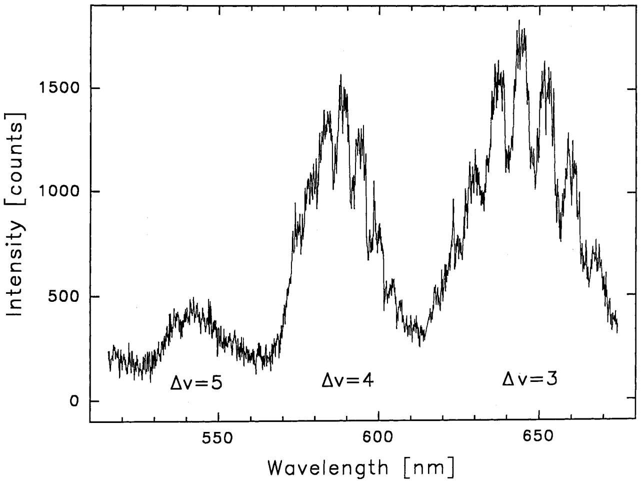

Figure 2. Survey spectrum of the N_2(B $^3\Pi_g \rightarrow$ A $^3\Sigma_u^+$) emission observed from collisional electronic energy transfer between metastable Kr atoms in a thermal beam and ground-state N_2 molecules in a gas cell.

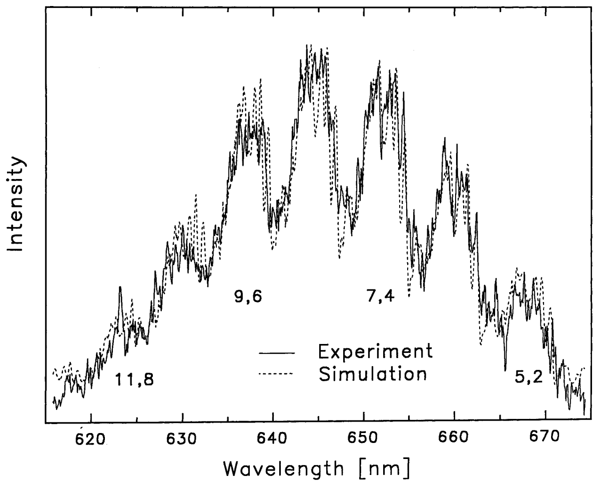

Figure 3. Experimental spectrum from Figure 2 (only $\Delta v = 3$ sequence, but on an expanded scale and with sensitivity correction), compared with an optimized computer-generated ("simulated") spectrum (dashed; see later in the text). Only every second band is labeled.

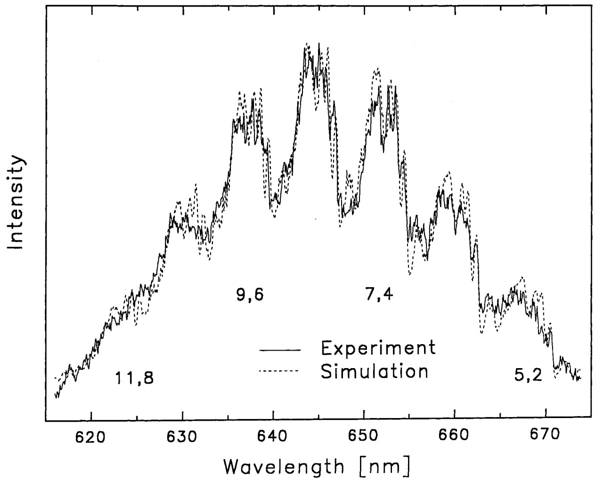

Figure 4. Spectrum of the $\Delta v = 3$ region as in Figure 3, but from Kr* + N_2 collisions at slightly superthermal energy ($E_{CM} = 94$ meV), and the corresponding simulation. The minima between the individual bands are clearly less deep than in Figure 3, due to higher rotational product excitation at the elevated collision energy.

instead of the Kr* + N_2 spectra. This afterglow[17] is a convenient means of generating a weak N_2(B−A) emission. Under the present conditions, for the same resolution (0.45 mm fwhm) and comparable S/N ratio, the Jarrell-Ash/OSMA detector yielded a spectrum in about $^1/_{50}$th of the time required with a $^3/_4$ m SPEX scanning spectrometer plus cooled PM tube. Generally the OSMA vs PM gain depends on the available photon flux and the required resolution.[18]

Each exposure of the OSMA with a fixed setting of the grating covered spectral intervals of ~60 and ~20 nm, using the small and the large spectrometers, respectively. Allowing these sections to overlap slightly made the exact setting of the grating less critical. The coarse wavelength calibration was done using a Ne lamp. This identified the channels of the diode array, for each fixed setting of the spectrometer grating, to within 0.2−0.3 nm. The exact matching of consecutive sections of the spectrum was done using the computer-simulated spectrum contours, as shown below. The relative spectral sensitivity of the diode array plus spectrometer and the transmission function of the fiber bundle were measured and, represented by polynomial fits, applied to the raw data to produce the corrected spectra given below.

III. Results

Figure 2 shows a low-resolution (0.45 nm fwhm) survey spectrum of N_2(B−A) emission from Kr* colliding with N_2 at 69 meV$_{CM}$ (unseeded beam). Three band sequences are covered, with $\Delta v = v' - v'' = 5$, 4, and 3. The intensities are here uncorrected for the spectral detector response; the dark current has been subtracted. This spectrum is a composite from three separate exposures. Most of the "grass" on the bands is not noise but results from resolved rotational and spin/orbit structure. Expanded plots of these same data (see below, Figure 3) reveal, for example, the characteristic triplet band heads. These details appear especially clearly in the high-resolution spectra given below (Figures 5−7).

The N_2(B−A) bands are shaded to the violet. In Figure 2, they exhibit extensive blending within each sequence. Qualitatively, this is clearly due to high rotational excitation of the emitting N_2 molecules. The overall appearance of this spectrum differs radically from that of the N_2(B−A) emission from rotationally cold N_2(B) molecules, such as was observed in the afterglow of excited nitrogen issuing from a nozzle discharge. For example, the spectrum shown in Figure 4 of ref 17, taken at about the same resolution (0.5 nm) as the present Figure 2, also shows emission from a broad vibrational distribution of N_2, $v' = 2$ to 6 in the $\Delta v = 2$ sequence. In this case, however, the bands are perfectly separated from each other, due to the low rotational excitation of the N_2 molecules in the beam. Figure 2 may also be compared with Figure 1b of ref 7, resulting from the reaction 2. This spectrum of the $\Delta v = 3$ sequence was obtained under similar conditions as in the present work (unseeded Kr beam, with slightly higher N_2 target pressure). Although it is considerably noisier, it shows in a qualitative way the same effect of high rotational excitation as observed here.

Figure 3 presents the data of the $\Delta v = 3$ region shown in Figure 2 on an expanded scale. Also, as in all subsequent figures, the intensity distribution has here been corrected for the spectral sensitivity of the detection system. For quantitative analysis, the method of spectrum simulation was employed. Vibrational term values for both N_2(A) and N_2(B) were obtained from the usual $v + {}^1/_2$ expansion, with molecular constants as determined by Geisen.[19] These are equivalent to the vibrational constants

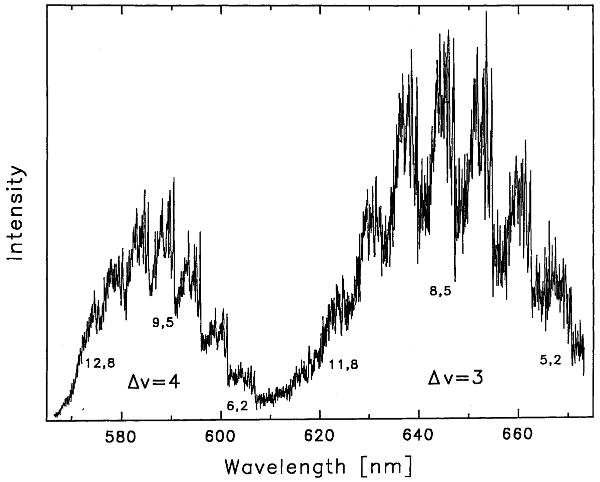

Figure 5. High-resolution survey spectrum of two sequences, observed at high collision energy (E_{CM} = 191 meV), sensitivity-corrected.

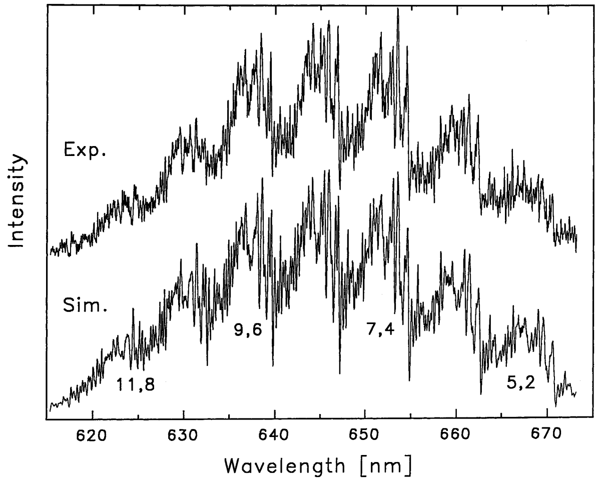

Figure 6. Expanded view of the $\Delta v = 3$ section of Figure 5 (top), compared with its high-resolution simulation (bottom).

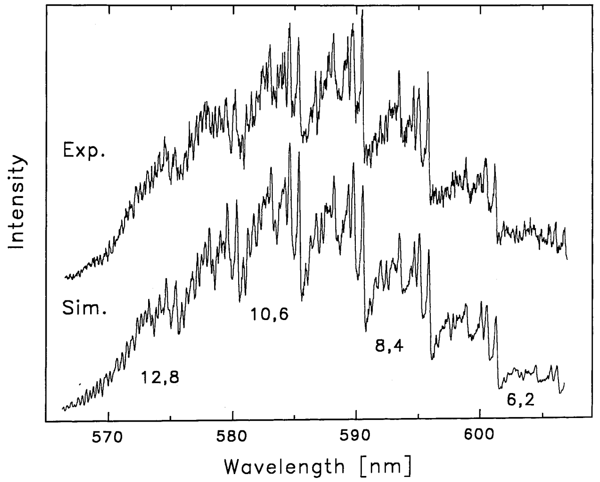

Figure 7. Same as Figure 6, for the $\Delta v = 4$ section from Figure 5.

given by Roux et al.[20] at low v' but are superior at high levels ($v' \sim 12$). The rotational term values were calculated by diagonalization of the A- and B-state Hamiltonian matrices from ref 20, using rotation and spin coupling constants as given therein. The rotational line strength factors were calculated from expressions given in Table 5.1 of ref 21 for pure Hund's case (a) functions; the J-dependent mixing of such pure states, to form the actual N_2(A) and N_2(B) eigenstates, was properly taken into account,[22,23] the mixing coefficients being obtained numerically as the eigenvectors from the above matrix diagonalizations. The intensities of the bands were weighted with $A_{v'v''}\cdot\tau(v')$, where $A_{v'v''}$ are the B → A emission Einstein coefficients, taken from ref 24, and $\tau(v')$ is the radiative lifetime as given in refs 25 and 26. The factor τ provides for the proper normalization to the sum of all other competing emissions, including the small fraction of B → W radiation.[24] Finally, in the simulation the apparatus resolution function was taken to be triangular with a slightly wider fwhm (0.5 nm) than that of the true, bell-shaped function (~0.45 nm). This allows for the broad but low wings that the real apparatus function exhibits. The calculation of the simulated spectrum was based on assumed relative vibrational and rotational distributions, which were adjusted by trial and error until an optimum visual overall fit of the synthetic spectrum with the experimental result was achieved. For convenience the rotational population was here described by a Boltzmann distribution with temperatures T_{rot}, dependent on v'.

Figure 3 shows the simulated spectrum arrived at in this way as a dashed line. It was obtained with a vibrational distribution $n_0(v')$ and rotational temperatures $T_{rot}(v')$ as given in Table 1, columns 4 and 7 (parentheses indicate a comparatively large uncertainty). These fit parameters and those for the other spectra constitute the essential results of this work, and their dynamical implications are discussed below.

Figure 4 shows the spectrum of the $\Delta v = 3$ sequence, taken with a (slightly) seeded Kr* beam (Kr:H_2 = 10:15 mbar), but otherwise the same conditions as for Figure 3. Even a qualitative inspection reveals important differences: the long-wavelength edges of each band are less sharply defined than in Figure 3; the minima between the bands are less marked relative to the peaks; there is relatively more intensity in the short-wavelength part ($\leq$635 nm) of the spectrum in Figure 4 than in Figure 3. All of these features point to a higher rotational excitation of the product for the increased collision energy. The spectrum simulation bears this out quantitatively: Table I, column 11 shows that T_{rot} is higher in each v' level by about 250 K. The vibrational population itself, on the other hand (Table I, column 8) does not depend much on the collision energy; there may be a slight enhancement of the higher v' levels in Figure 4 (at 94 meV$_{CM}$), compared to that in Figure 3 (for 69 meV$_{CM}$), but the difference is on the order of the error limits.

An interesting result is the higher intensity of the N_2 emission under the seeded conditions. The peak intensity was ~1400 cts in Figure 3 and ~2500 cts in Figure 4. Taking into account the data acquisition times of 20 and 8 min, respectively, the intensity increase upon seeding amounts to a factor of 4.5. In the earlier work on Xe[15] it was found that seeding increased the metastable atom flux very considerably; using a 1:5 Xe:H_2 pressure ratio, the beam intensity increased by a factor of 13 compared to an unseeded beam. This may be attributable to a concentration of Xe* atoms on the beam axis through collisions with the H_2 molecules. In the present work, the Kr* flux with and without seeding was not measured directly. It is therefore impossible to decide to what extent the observed increase in N_2(B) emission is due to a higher Kr* flux or, alternatively, to a rise of the energy transfer cross section. However, the very large enhancement of metastable flux that can be achieved with Xe suggests that most, if not all, of the Kr* "seed gain" factor of 4.5 observed in this work, using milder seed conditions, is also due to an enhanced Kr* flux. Unfortunately, the intensity measured with the higher seed ratio at 190 meV$_{CM}$ cannot be related to those given above, because in this experiment the high-resolution monochromator was used.

The spectrum shown in Figure 5 is a composite of seven exposures, taken at high resolution (0.15 nm fwhm) and with the 16:34 mbar Kr:H_2 seed ratio. A rather wide overlap of adjacent sections (5 nm on each side) ensured a perfect relative positioning. As in Figure 2, the fine structure is largely reproducible and is therefore clearly not due to noise. The two sequences shown, $\Delta v = 4$ and $\Delta v = 3$, include the bands (12,8) to (6,2) and (11,8) to (5,2), with heads near 576−607 nm and 625−670 nm, respectively. Note the steep intensity decrease to the left of the (12,8) band, at 570 nm. This effect, which can also be seen in Figure 2, demonstrates the well-known predissociation of the B-state level with $v' \geq 13$. In contrast, in the $\Delta v = 3$ sequence the intensity falls off much more gradually to the left of the (11,8) band, i.e., in the region 610−620 nm, where there is some contribution from (12,9) emission.

The correction for the spectral response of the apparatus was more severe for the results obtained with the high-resolution spectrometer. Roughly, the sensitivity in the region of $\Delta v = 3$ was about half of that in the $\Delta v = 4$ sequence. The consistency of the intensity corrections can be checked on the basis of the known branching ratio between two bands from the same v' level, e.g. (9,5) at 589 nm and (9,6) at 638 nm. From the respective Einstein coefficients[24] one finds a (9,5):(9,6) intensity ratio of 0.69. The observed ratio is 0.62. The agreement is very satisfactory, considering the experimental error limits.

Expanded views of the same data as in Figure 5, are shown at the top of Figures 6 and 7 for the separate $\Delta v = 3$ and $\Delta v = 4$ regions, respectively. Below them, the corresponding computer simulations are given. The apparatus resolution function was again assumed to be triangular with a slightly broadened fwhm (0.2 nm vs 0.15 nm), as was done in the low-resolution simulations, Figures 3 and 4. Note that the (12,9) band does not appear in Figure 6, because it is too weak on account of a small Einstein coefficient. The (12,8) band is much stronger (cf. Figure 5); therefore only the $\Delta v = 4$ sequence, Figure 7, gives useful information on the population of the $v' = 12$ level. On the other hand, $v' = 5$ contributes only to the $\Delta v = 3$ sequence, Figure 6. The population of $v' = 4$ can, as in Figures 3 and 4, only be inferred with a rather large uncertainty, by means of the short-wavelength tail of the (4,1) band extending into the (5,2) band.

The relative vibrational populations obtained from the two independent fits shown in Figures 6 and 7 were identical for $v' = 6-10$, and for $v' = 11$ they differed only insignificantly (0.40 vs 0.35), averaged to 0.37). They are given in Table 1 column 12. Both simulations were also done with the same set of $T_{rot}(v')$ values, Table 1, column 13.

In summary, a comparison of the experimental and the synthetic spectra demonstrates that nearly all of the observed fine details are real features, resulting from partially blended rotational lines belonging to the 27 branches of this complex $^3\Pi-^3\Sigma$-electronic transition.

IV. Error Analysis

1. Rotational Distributions. The detailed structure of the bands, such as is shown in Figures 6 and 7, might conceivably be affected by partial rotational relaxation of N_2(B) in collisions with the N_2(X) reactant gas molecules at the relatively high density of 10^{14} cm^{-3} used. An estimate shows, however, that this effect is negligible. Katayama has studied rotational relaxation of N_2(B,v=3,J=(0 and 7)) by collisions with Ar at 2.5 Torr and 300 K using a pump-and-probe technique.[27] Although absolute cross sections were not measured, the spectra given in ref 27 show that within 25 ns the rotational transfer out of the initially populated level is ~45% for $J = 0$ and ~27% for $J = 7$. This translates into total rotational transfer cross sections of 68 and 36 Å^2, respectively. Cross sections in the 50−100 Å^2 range for this type of process have also been measured for other electronically excited molecules colliding with rare gases and H_2 (e.g., for I_2(B),[28,29] Na_2(B),[30] Li_2(B),[31,32] and Li_2(A)[33]). As an example of a heavy molecular collision partner, the I_2(B) + I_2 system was studied in ref 28, and total rotational transfer cross sections of 76 and 45 Å^2 were found at an initial J of 33 and 103, respectively.

Assuming, then, for the present system N_2(B) + N_2 a cross section of 50 Å^2, one calculates a rate of 2.5×10^4 s^{-1} for collision-induced rotational relaxation under the conditions used. This is slow compared to the radiative rate of 2×10^5 s^{-1}.[25,26] Thus only ~12% of the excited molecules are expected to suffer such collisions before radiating. Moreover, most of these collisions change the rotational state by only two or four units of J (for larger ΔJ the cross sections are much smaller,[27,30,33] which is insignificant for the broad J-distributions observed in this experiment (for $T_{rot} = 1500$ K, the most probable J is $J_{mp} = 18$).

2. Intensity Corrections. The measured N_2(B−A) band intensities have to be corrected to allow for the fact that some N_2(B) molecules emit outside of the observation region. Since the exothermicity of reaction 2 for formation of the low vibrational levels of the N_2(B) product is considerable, while at the same time the radiative lifetime of the low levels is longer, the fraction of undetected N_2(B,v') molecules is greater for low than for high v'. The factors CF(v') listed in Table 1 correct approximately for this loss of luminescence light. They were obtained as follows.

First the mean exothermicity $\Delta E(v')$ for a particular v' level was calculated, taking into account the observed rotational product excitation:

$$\Delta E = \Delta E_0 - E_{rot}$$

Here

$$\Delta E_0 = E(\mathrm{Kr}(^3P_2)) - E(N_2(B),v')$$
$$= 9.915\ \mathrm{eV} - hc[T_e + \omega_e(v' + {}^1\!/_2) - \omega_e x_e(v' + {}^1\!/_2)^2]$$

is the nominal exothermicity for rotationless product.

$$E_{rot} = hcB_{v'}J(J + 1)$$

with

$$J = J_{mp} = 0.5896\sqrt{T_{rot}(v')/B_{v'}} - {}^1\!/_2$$

was taken as the rotational energy of N_2(B,v'). It amounts to only 50−70 meV, depending on v' and the seed condition, while ΔE varies from 0.26 to 1.74 eV over the v' range considered; see Table 1. The vibrational level $v' = 13$, which is near-resonant ($\Delta E = 0.09$ eV) with Kr($^3P_2$), is not included here because N_2(B) is strongly predissociated for $v' > 12$.[34]

The translational N_2(B) energy is, from the mass ratio,

$$E_{N_2(B)} = \frac{m_{Kr}}{m_{Kr} + m_{N_2}}\Delta E = 0.75\Delta E$$

in the center of mass frame, corresponding to CM velocities

TABLE 1: Vibrational−Rotational Population Distributions of N_2(B) Produced by Kr* + N_2 Collisions

			E_{CM} = 69 meV				E_{CM} = 94 meV				E_{CM} =191 meV				
v'	ΔE^a (eV)	τ^b (μs)	$n_o(v')^c$	CF^d	$n(v')^e$ corr	T_{rot}^f	$n_o(v')^c$	CF^d	$n(v')^e$ corr	T_{rot}^f	$n_o(v')^c$	CF^d	$n(v')^e$ corr	T_{rot}^f	$n(v')^g$
12	0.261	4.0		0.57			(0.21)	0.64	(0.13)		0.18	0.71	0.13	1400	0.33
11	0.433	4.1	0.38	0.65	0.25	1100	0.40	0.69	0.28	1350	0.37	0.75	0.28	1450	0.40
10	0.608	4.3	0.57	0.74	0.42	1150	0.63	0.75	0.47	1400	0.65	0.80	0.52	1500	0.72
9	0.787	4.5	0.86	0.82	0.70	1200	0.87	0.83	0.72	1400	0.86	0.85	0.73	1500	0.86
8	0.970	4.8	0.95	0.88	0.84	1250	0.98	0.90	0.88	1450	0.93	0.89	0.83	1550	0.97
7	1.156	5.1	1.00	1.00	1.00	1250	1.00	1.00	1.00	1500	1.00	1.00	1.00	1600	1.00
6	1.346	5.5	0.88	1.14	1.00	1300	0.86	1.11	0.95	1550	0.85	1.08	0.92	1650	0.76
5	1.540	5.9	0.75	1.25	0.94	1300	0.68	1.20	0.82	1650	0.82	1.19	0.97	1750	0.64
4	1.737	6.5	(0.60)	1.41	(0.84)		(0.63)	1.37	(0.86)		(0.60)	1.30	(0.78)		0.56

[a] Mean exothermicity for reaction into the N_2(B) vibrational level v' (see text). [b] Radiative lifetime of $N_2(B,v')$, from ref 25. [c] Relative vibrational level populations as derived from spectrum simulation (raw data). [d] Correction factors (see text). [e] Corrected vibrational level population, $n(v') = CF{\cdot}n_o(v')$. [f] Best-fit rotational "temperatures" as derived from spectrum simulation. [g] Relative vibrational level population from ref 7.

$u_{N_2(B)}$, which range from ~1000 m/s for $v' = 12$ to 3000 m/s for $v' = 4$. Newton diagrams were then considered for the three Kr* lab-frame velocities used, 530, 790, and 1240 m/s (corresponding to the Kr* lab system energies given above for the three seed conditions) and for isotropically distributed mean velocities of the N_2 target molecules (475 m/s at room temperature). The product N_2(B) was assumed to be scattered strictly forward in the CM system (the assumption of strictly backward scattering would give almost identical results; for 90° sideways scattering, too, the results would be the same for the unseeded beam, and only for the seeded conditions would the correction then be somewhat greater). The average lab system N_2(B) velocity component $v_\perp$ perpendicular to the Kr* beam direction was then estimated from $u_{N_2(B)}$ and the Newton diagram geometry. Let $y_0 = v_\perp \tau$ be the mean distance that the N_2(B) molecules travel away from the beam axis during their radiative lifetime τ. With the observation region extending to $\pm y_{max}$ on either side of the beam axis, the fraction of detected products will be

$$(CF)^{-1} = \frac{\int_0^{y_{max}} \exp(-y/y_0)\, dy}{\int_0^{\infty} \exp(-y/y_0)\, dy}$$

For the fiber bundle optics used in the present experiment, y_{max} = 6 mm.[15] This gives the correction factors CF listed in Table 1, where they are normalized to unity at $v' = 7$. It can be seen that the most serious light losses occur for the lowest Kr* velocity (because the Newton diagram geometry gives then the greatest $v_\perp$ component). In this worst case the corrections for the highest and lowest v' amount to ~±40% relative to $v' = 7$.

3. Statistical Uncertainty. The final, optimum fit spectrum simulations shown in Figures 3, 4, 6, and 7 were arrived at after about 10 iterations each. The fine adjustment of the relative vibrational population was made in steps of 0.03 (relative to 1.00 for $v' = 7$), and that of T_{rot} in steps of 50 K. However, on this grid adjacent fits showed almost no discernible differences. The error limit is therefore estimated to be about ±0.05 for $n(v')$ and ±100−150 K (depending on v') for T_{rot}. The relative population of the three fine-structure components $^3\Pi_{0,1,2}$ of N_2(B) was taken to be the same. Some tests were carried out to detect a possible unequal population of these levels, such as has been observed in some cases with Xe* + N_2[35,36] and Xe* + CO.[37] 10 different deviations from a 1:1:1 population ratio were tried, differing by up to factors of three, similar to what was found for Xe* + N_2. The effect of these variations on the simulated spectra was, however, still within the bounds of the experimental noise, so that nothing can be stated about any propensity for certain fine-structure levels. It is to be noted, however, that in both the Xe* + N_2 and the Xe* + CO case the product rotational temperature was much lower (T_{rot} = 300−450° K); the spectrum contour then responds much more sensitively to a variation of the relative fine-structure level population.

V. Discussion

1. Kr Reactant State. It is to be expected that the metastable krypton beam used in the present experiment consisted of a mixture of Kr($^3P_2$) and Kr($^3P_0$) atoms, having excitation energies of 9.915 and 10.56 eV, respectively. In our earlier experiments with metastable Xenon from the same beam source,[9] the higher state Xe($^3P_0$) was found to be significantly populated.[38] A metastable Kr atom beam from a cold cathode discharge has been measured (by photon electron spectroscopy combined with laser pumping) to contain about 9% Kr($^3P_0$).[39] Even under flow conditions a similar relative $^3P_0$ concentration could be achieved, provided He carrier gas was used.[40] However, in the latter work it was also shown that reactions of Kr($^3P_0$) with nitrogen do not give rise to any luminescent product. Using CW dye laser pumping, 30% of the Kr($^3P_2$) atoms could be converted to Kr($^3P_0$), but this did not affect the spectral distribution. In a similar study,[41] despite a careful search, the authors were "unsuccessful in identifying any N_2* emission from the Kr($^3P_0$) + N_2 reaction". Very likely, these collisions lead to predissociated states of N_2. In any case, it is justified to ascribe the observed luminescence in this work entirely to Kr($^3P_2$) collisions, eq 2.

2. Direct vs Indirect N_2(B) Population. The possibility was considered that initially the energy transfer from Kr($^3P_2$) occurs not to the N_2(B $^3\Pi_g$) state directly, but to the N_2(W $^3\Delta_u$) state, which can radiate in the IR into N_2(B).[17] The observed N_2(B−A) emission might then be the second step of a cascade; see Figure 1. The N_2(W) vibrational states in the vicinity of the Kr($^3P_2$) energy (9.915 eV) are v' = 13−16, having energy separations from this energy level of −0.264, −0.121, +0.019, and +0.156 eV, respectively (calculated with the molecular constants of N_2(W) given in ref 42). If the hypothetical energy transfer from Kr($^3P_2$) into N_2(W) populated preferentially the nearest-to-resonance, slightly endoergic vibrational level, analogous to the energy transfer from Xe($^3P_2$) into $N_2(B,v'{=}5)$,[9] then $N_2(W,v{=}15)$ would be the dominant product level. The emission branching ratios into various N_2(B) levels are well-known from the N_2(B−W) radiative transition probabilities given in ref 17, Table 2. They are based on accurate ab initio calculations of the B−W transition moment.[24] Figure 8 shows the expected N_2(B) vibrational population resulting from IR radiative transitions out of the $N_2(W,v{=}15)$ level (solid line). The dots give the N_2(B) vibrational population observed in this experiment (here for the case of strong seeding, and after correction with

TABLE 2: Rotational Temperature (K) of $N_2^*(v')$ Product from Three Electronic Energy Transfer Reactions

		CM collision energy	
	v'	56 meV	300 meV
$Xe^* + N_2 \rightarrow Xe + N_2(B, v')$[a]	4	3500	5000
	3	900	1700
	2	700	700
	1	600[b]	450

		CM collision energy		
	v'	69 meV	94 meV	191 meV
$Kr^* + N_2 \rightarrow Kr + N_2$ (B, v') (this work, see Table 1)	12			1400
	11	1100	1350	1450
	10	1150	1400	1500
	9	1200	1400	1500
	8	1250	1450	1550
	7	1250	1500	1600
	6	1300	1550	1650
	5	1300	1650	1750

		CM collision energy		
	v'	65 meV[c]	76/89 meV[d]	161 meV[d]
$Ar^* + N_2 \rightarrow Ar + N_2$ (C, v')	3	130		
	2	370		
	1	1010		(4000)[e]
	0	1960[f]	1700/1600	2200

[a] Reference 10; the data on $^{15}N_2$ are also given. [b] Probably too high; for $^{15}N_2(v{=}1)$, ref 10 gives $T_{rot} = 350$ K at both energies. [c] Reference 2. [d] Reference 12. [e] Very uncertain, bimodal. [f] Reference 13 gives at ~60 meV a bimodal distribution in $v' = 0$.

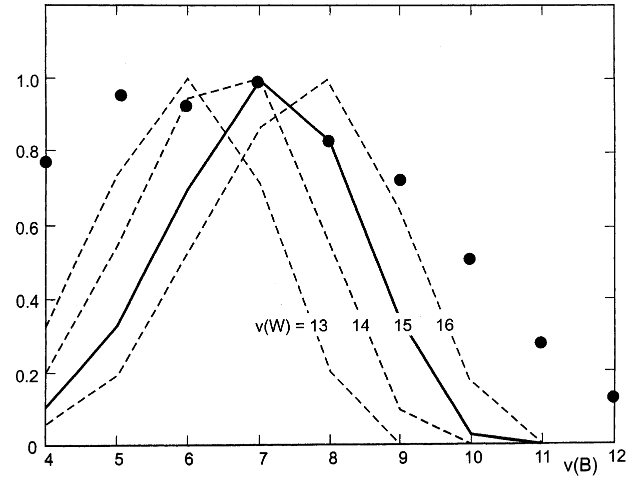

Figure 8. Dots: observed relative vibrational population distribution P_{vib}, as extracted from the high-resolution spectra ($E_{CM} = 191$ meV), using corrections as described in the text. Solid line (normalized at the peak to the highest experimental point): calculated P_{vib} distribution of $N_2(B)$ assuming that the B state is not populated by direct E−E-transfer from $Kr(^3P_2)$, but instead by a secondary process via the $N_2(W\ ^3\Delta_u)$ state. Specifically, for the solid line it was assumed that initially only the $v = 15$ level of the W state was populated in a near-resonant E−E-transfer from $Kr(^3P_2)$, while the $N_2(B,v')$ levels are then populated radiatively from $N_2(W,v{=}15)$. The dashed lines were calculated similarly, assuming primary excitation of the somewhat off-resonance levels $N_2(W,v{=}13,14,16)$ as indicated. It is concluded that none of these hypothetical processes can explain the observed $N_2(B)$ P_{vib} distribution.

CF; see Table 1, third block of data). The comparison shows that the observed and the "predicted" distributions agree only at the peak at $v(B) = 7$ and also at $v(B) = 8$, but otherwise the calculated distribution is far too narrow. To test for the possibility that W-state levels other than $v = 15$ are initially populated, Figure 8 also gives the $N_2(B)$ distributions expected in the case that the adjacent levels $v(W) = 13$, 14, and 16 are responsible (dashed lines). Again, each of these distributions individually is not nearly broad enough to be consistent with the observation. Even a superposition of several of them cannot explain the experimental distribution in the region $v(B) = 9-12$. These levels could only be populated by radiation from W-state levels higher than $v(W) = 16$, which, however, are not energetically accessible.

Analogously one might also consider the $N_2(B'\ ^3\Sigma_u^-)$ state as a possible precursor to the B-state population. Here the $v(B') = 11$ level, slightly (0.125 eV) endoergic with respect to $K(^3P_2)$, might be initially selectively populated. The $N_2(B'-B)$ Einstein coefficients are given in ref 24, Table XIII. They show that B′, $v = 11$ emission would produce a B-state vibrational distribution that is completely inconsistent with that observed here. It peaks at $v(B) = 5$ and 6, $v(B) = 7$ receives only ~26% of the peak population, and the population of $v(B) = 8-12$ is oscillatory and less than 10% of the peak. Assuming an initial slightly exothermic energy transfer into $N_2(B',v{=}10,9)$, the resulting B-state distribution would peak sharply at $v(B) = 5$ or 4, respectively, with $v(B) = 7$ having only a few percent of the peak population. Again there is no way of explaining the observed excitation of $N_2(B,v{=}9-12)$ via emission from the B′ state in any of its energetically accessible levels.

Thus we conclude that radiative cascades, either via $N_2(W)$ or via the $N_2(B')$ state, cannot make significant contributions to the observed $N_2(B)$ population. The dominant, and probably only excitation mechanism of $N_2(B\ ^3\Pi_g)$ must be the direct energy transfer from $Kr(^3P_2)$.

3. Curve Crossing Mechanisms. *A. Simplified Model: Purely Repulsive Entrance Channel Potential.* The $Kr^* + N_2$ reaction (2) is intermediate between the related reactions (1) for Ar* and (3) for Xe*. This is graphically demonstrated in Figure 9, which illustrates a possible reaction mechanisms and is a guide toward an interpretation of the experimental results.

Panels a−c of Figure 9 refer to the $Rg^* + N_2$ reactions (1)−(3) and show the respective potential energy curves semischematically. The entrance channel curves are given for the lower metastable species $Rg^*(^3P_2) + N_2$ in each case. They are represented here by purely repulsive potentials, as is suggested by a simple charge overlap model.[43] This model considers the overlap of the electron density distributions of $N_2(X\ ^1\Sigma_g^+)$ and the outermost atomic orbital, *n*s, of Rg* (*n* = 4, 5, 6 for Ar*, Kr*, Xe*, respectively). For the case of Xe*, the resulting potential has been calculated in ref 9. Refinements have been given in ref 9 and particularly in ref 11 and will be considered below. The rise of the repulsive branch in Figure 9c is taken, qualitatively, from Figure 5 in ref 9. It corresponds to the onset of the overlap with the charge density distribution of the Xe* 6s electron, which is given in Figure 9c, bottom (from ref 15, Figure V.5). This density peaks at 2.50 Å and extends out to 3.60 Å (50% of peak value) from the Xe nucleus. The repulsion along the $Xe^* + N_2$ potential curve is thus taken to set in just slightly outward from the 3.60 Å point, at about 4.0 Å (Figure 9c), in agreement with the quantitative curve shown in Figure 5 of ref 9.

The exit channel potential for reaction (3) was modeled similarly in ref 9 and is also shown as a repulsive curve in Figure 9, for the dominant $N_2(B)$ vibrational level $v' = 5$. The construction of the repulsive part of the exit potential is explained in ref 9. The two curves intersect at a point marked by a dot.

The third, attractive curve shown in Figure 9 gives the ionic N_2^-/Xe^+ Coulombic potential, as discussed in greater detail in ref 11. It is defined by its asymptotic value for $Xe^+(^2P_{3/2})$ +

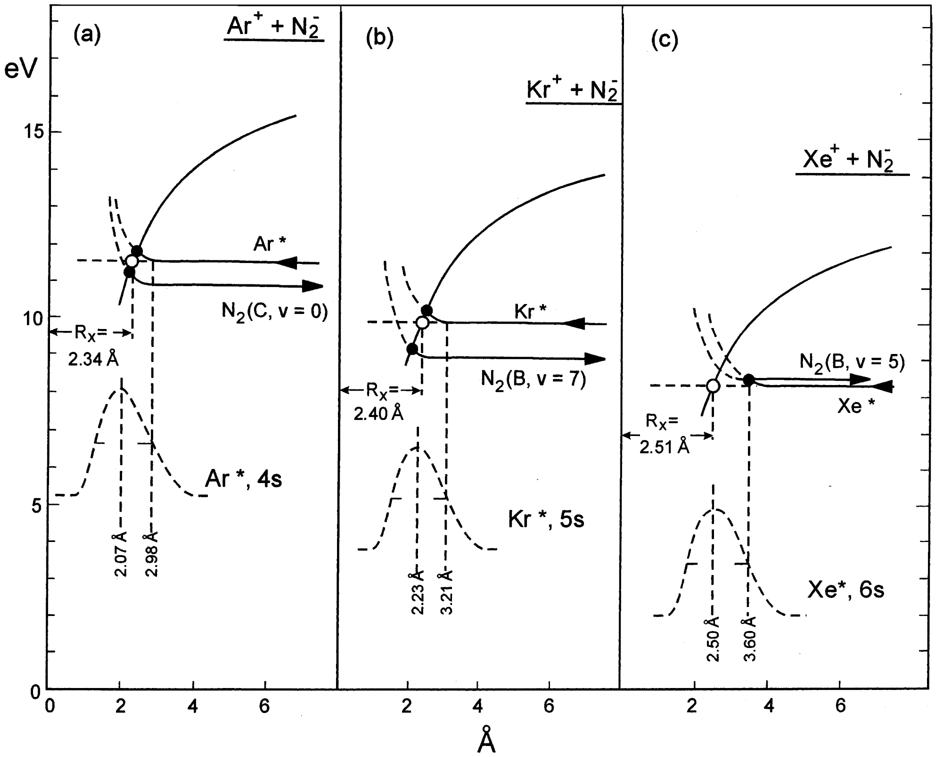

Figure 9. Diagrams explaining the two possible E−E transfer mechanisms, “covalent−covalent” vs “ionic intermediate”, for the Ar* + N_2, Kr* + N_2, and Xe* + N_2 reactions ((a)−(c)). Entrance and exit channel potentials are marked by arrows, the third, steep curve in each case is the Rg^+ + N_2^- ionic (Coulombic) curve. Its crossing radius R_x, where charge transfer between the reactants would be thermoneutral, is marked by a small circle. Dots mark the covalent curve crossings. The dashed curves show the charge density distributions of the 4s, 5s, 6s electrons ((a)−(c)), the outer limbs of which determine the onset of covalent repulsion. Panel c is based on model calculations, (a) and (b) are obtained by scaling to (c) (for details, see text). Important refinements, such as the splitting of the entrance potential into a repulsive branch, as shown, plus two attractive branches (omitted here) are discussed later in the text (section V.3.B).

N_2^- (X $^2\Pi_g$) shown in Figure 9c, top right. This asymptote is located at the energy IP(Xe) − EA(N_2), with the ionization potential being IP = 12.13 eV and the electron affinity EA = −1.90 eV.[44] Its intersection with the extrapolated asymptotic Xe* + N_2 entrance potential (dashed horizontal line) is marked by a circle, at R_x = 2.51 Å. This value is very close to the peak of the Xe*(6s) distribution and is thus deep inside the repulsive region of the Xe* + N_2 interaction. The crossing between the Xe* + N_2 repulsive branch and the Xe^+ + N_2^- attractive curve, at which point the charge transfer, if any, would have to occur, lies far too high to be accessible at the collision energies used. Thus in reaction 3 an ionic intermediate certainly plays no role; the energy transfer to form N_2(B) takes place entirely by a covalent/covalent nonadiabatic curve crossing mechanism, at the point marked by the dot.

Panels a and b of Figure 9 are organized in the same way as (c). The entrance channels are again purely repulsive, the repulsion setting in near the outer 50%-of-peak point of the 4s electron (for Ar*) and 5s electron (for Kr*) density distributions shown at the bottom. Lacking precise information on these distributions, they were here simply scaled down radially, relative to that for Xe* in panel (c). The scale factors used are the ratios of the atomic radii $\langle r \rangle$ of the corresponding alkali atoms K, Rb, and Cs in their ^2S ground states, which are 2.77, 2.98, and 3.34 Å, respectively.[45]

The exit channel potentials are shown for the experimentally observed, dominant product vibrational level, i.e., $N_2(C,v'=0)$ for Ar* + N_2 and $N_2(B,v'=7)$ for Kr* + N_2 (see Figure 8). The shape of their repulsive parts, which is not very critical for the present purpose, is schematic. The vibrational product levels v' = 1 and 2 in (a) and v' = 8−13 in (b) would be located between the entrance and exit channel curves shown. There are here *no* covalent/covalent crossings, even if the relative radial positions of the entrance and exit repulsive portions were different from those shown. It is certain in any case that the repulsive wall of the entrance channels, Rg* + N_2, lies at *greater* reactant separation than that of the exit channels, Rg + N_2(B or C), since the position of the former is controlled by the “inflated” radius of the excited *n*s electron.

The ionic curves, however, drawn in Figure 9a,b analogously to Figure 9c, do offer a reaction pathway from the entrance to the exit channels. *Two* subsequent nonadiabatic transitions are required here, at the crossing points marked by dots. It is instructive to compare the radial position of the ionic curves relative to the covalent entrance channel repulsion. The locations of the Rg^+−N_2^- curves are characterized essentially by the points where they intersect the Rg* + N_2 energy level (marked by small circles in each panel of Figure 9, and labeled as R_x). The Rg* + N_2 repulsive region, on the other hand, is summarily best described by the peak position of the Rg* *n*s electron density, also labeled in the figure. It is then seen that for Xe* + N_2 the two values are nearly equal (2.51 and 2.50 Å, respectively). For Kr* + N_2, R_x is somewhat greater than the *n*s peak density radius (2.40 vs 2.23 Å), and this trend continues to Ar* + N_2 (2.34 vs 2.07 Å). Thus for Xe*, the ionic crossing radius R_x is dynamically inaccessible, being “shielded” by the repulsion further out. This reaction proceeds therefore entirely along covalent curves. For the Ar* + N_2 system, as the other extreme, R_x is reached during the collision outward from the region of strong covalent repulsion. This reaction, therefore, occurs via an Ar^+ + N_2^- ion pair stage. The case of Kr* + N_2 is intermediate. The crossing radius R_x would appear to be accessible as with $Ar^* + N_2$, but it is located well within the tail of the covalent repulsion. Correspondingly, the intersection of the $Kr^* + N_2$ and $Kr^+ + N_2^-$ curves lies rather high in energy above the entrance channel asymptote (see the upper dot in Figure 9b). Thus a considerable activation energy is expected for this reaction. This may well explain the strikingly small luminescence cross section in this case, which made the present experiment so difficult (see above). Even for $Ar^* + N_2$ evidence for a very small activation energy of this type has been obtained in flowing afterglow experiments at 90 K vs 300 K.[13]

B. Refinement: Attractive Entrance Potential Components. The ionic intermediate in the Ar* and $Kr^* + N_2$ reactions leads quite naturally to low vibrational product levels, with considerable reaction exothermicity. This has no counterpart in the $Xe^* + N_2$ case; therefore $N_2(B)$ levels below the resonant level $v' = 5$ would not be expected to be populated.

However, some emission from $v' = 1-4$ is in fact observed, albeit with much lower intensity ($\leq 20\%$) than from $v' = 5$ (see the revised results given in ref 10, which supersede the early data from ref 9). To explain these product channels, two important refinements of the crude potential model of ref 9 are presented in ref 11: (a) The partial penetration of the target electron cloud through the Xe 6s shell was included. This exposes the target to the Xe^+ $5p^5$ core and leads to an additional *attractive* interaction. (b) The electronic anisotropy of the Xe($^3P_2$) atom was considered. The three different orientations of the $J = 2$ angular momentum with respect to the Xe^*-N_2 axis lead to a splitting of the entrance channel potential into three branches, which was ignored in ref 9. Briefly, expanding the potential around a P-state atom into spherical harmonics, the anisotropic (second) term is found to be $V_2 = {}^5/_2(V_\Sigma - V_\Pi)$, where V_Σ and V_Π are the electrostatic potentials for the Σ and Π orientation of the Xe $5p^5$ shell with respect to the Xe^*-N_2 axis (in collinear geometry). Diagonalizing the total Hamiltonian, inclusive of spin, then yields the *three* adiabatic potentials V_{20}, V_{21}, and V_{22}, which govern the collision. They are approximately obtained as the simple expressions $V_{20} = V_0 + {}^1/_5V_2$, $V_{21} = V_0 + {}^2/_5V_2$, and $V_{22} = V_0 - {}^1/_5V_2$ (eqs 12, 14, and 16 in ref 11). V_0 is the isotropic (first) term of the potential expansion and is identified with the potential from ref 9, but with the above modification (a) (ref 11, Figure 1). V_2 is a negative term; hence the ordering of the three branches is V_{22} (top), V_{20} (middle), and V_{21} (bottom), as shown in Figure 2 of ref 11. This figure illustrates the important result that, for perpendicular N_2-Xe^* collision geometry, the branches V_{20} and V_{21} do provide a path toward the exothermic product channels $N_2(B,v'<5)$.

In Figure 9, the splitting of the entrance channel potentials has for clarity been omitted in all three systems. However, the modifications (a) and (b) (inclusion of a partially shielded ion-induced dipole, and the splitting into the three branches V_{20}, V_{21}, and V_{22}) will give a qualitatively similar picture for $Kr^* + N_2$, as is shown in ref 11, Figure 2, for $Xe^* + N_2$. The possibility therefore exists that in the present study the highly exothermic product channels $N_2(B,v'=4-12)$ are, in fact, populated via entirely covalent potential curves, and not via an intermediate ion-pair state. The small luminescence cross sections for this reaction could then be explained similarly as was the weak $v' = 4, 3, 2, 1$ emission in the $Xe^* + N_2$ case. Symmetry arguments presented in ref 11 show that in a rough approximation the path via V_{21} does not contribute at all, and V_{20} only with a statistical weight 7 times smaller than that of V_{22}. V_{22}, on the other hand, being repulsive, would in the $Kr^* + N_2$ case only populate $N_2(B)$ levels $v' \geq 13$, which are predissociated and unobservable. The observed levels $v' \leq 12$ would all be due to the statistically heavily disfavored V_{20} path.

4. Dynamics of the $Kr^* + N_2$ Reaction vs Ar* and $Xe^* + N_2$. It is informative to compare the present results on the rovibrational population distribution of the N_2^* product with the corresponding data on the $Ar^* + N_2$ and $Xe^* + N_2$ systems. One might expect to obtain a clue as to whether Kr* behaves similarly to Xe*, i.e., controlled by covalent forces, or whether it involves an ionic intermediate, as Ar* does.

The observed vibrational distributions, P_{vib}, are bewilderingly different. Kr* leads to a clear enhancement of $N_2(B)$ vibrational levels in the middle of the accessible range (see Table I and Figure 8), with no significant dependence on the collision energy. Ar* impact populates only four vibrational levels of $N_2(C)$, i.e., $v' = 3$, 2, 1, and 0[2]. The relative population rises here sharply in the above order, 0.3, 3.0, 16, 100 at 65 meV collision energy,[2] but very similarly also at superthermal energies.[3] Finally, the Xe*($^3P_2$) data show for $N_2(B)$, apart from the strong enhancement of the resonant $v' = 5$ level, a minimum of P_{vib} (relative to $P_{vib} = 100$ for $v' = 5$) at $v' = 3$: $P_{vib} = 20$, 11, 17, 20 for $v' = 4-1$, averaged over $^{14}N_2$ and $^{15}N_2$ and also over the energies 56 and 300 meV, on which P_{vib} again depends very little.[10]

Since P_{vib} for $Kr^* + N_2$ resembles neither the $Ar^* + N_2$ nor the $Xe^* + N_2$ distributions, it is not possible to answer the "ionic vs covalent" question on this basis. The only similarity concerns the remarkable insensitivity against variations of the collision energy, but then all three systems share this feature. Thus again, this comparison is not helpful in arriving at a decision.

For the $Xe^* + N_2$ system, a detailed theoretical treatment of the P_{vib} distribution has been given.[46] The transitions from the entrance channel to a given $N_2(B,v')$ exit channel, both modeled by the potentials from ref 11, are treated as sequences of Landau−Zener processes at each traversed crossing point. With little adjustment of the parameters, the experimental P_{vib} distributions reported in ref 9 could be well reproduced. The improved, slightly revised data from the later experiments[10] could no doubt have been fitted equally well.

Similar treatments of the Ar* and $Kr^* + N_2$ reactions have not been made. Certainly for Ar*, and perhaps also for Kr*, the assumed potential model would have to be entirely different from the Xe case, to incorporate the ionic intermediate. The success or failure of such a model for $Kr^* + N_2$ could then help to decide on the presence or absence of a transient ion-pair state in that case.

Another, potentially promising approach toward a decision on the type of the $Kr^*+ N_2$ energy transfer process is a comparison of the observed rotational distributions in the three systems, as expressed summarily by the "temperature" T_{rot} of the respective Boltzmann fits. Table 2 presents this comparison. It can be summarized as follows. (a) In practically all cases T_{rot} increases with increasing collision energy E_{CM}. (b) With increasing exothermicity, i.e., from the high to the low vibrational levels, T_{rot} *increases* in the Ar* and Kr* cases but *decreases* (!) in the Xe* reaction.

The property (a) is intuitively plausible. At higher impact energy the total angular momentum of the collision pair will also be greater, and it is reasonable to expect that after the collision the N_2^* product will internally be more rotationally excited, too.

The finding (b) appears to indicate that the sequence of curve crossings through which the reaction path filters down from the entrance level to a given vibrational exit level is similar in the $Ar^* + N_2$ and $Kr^* + N_2$ cases, but very different from that in the Xe* + N_2 reaction. This lends some support to the idea that the Kr* + N_2 reaction 2 is of the ionic-intermediate type like the Ar* + N_2 collision (1), and fundamentally different from the covalent mechanism of Xe* + N_2 reaction 3.

The theoretical treatment in refs 11 and 46 did not consider the T_{rot} distribution, apart from some qualitative remarks. For example, the preferred collision geometry for population of the $N_2(B,v'<5)$ levels was shown to be perpendicular, consistent with the high rotational product excitation which the then available coarse data on T_{rot}[15] showed. The later, much more precise data from ref 10 revealed clearly the surprising, *de*creasing trend of T_{rot} in going from $v' = 4$ to 1 (Table 2), but these results were not available at the time of the work of ref 11, and there is up till now no theoretical analysis of this feature.

This is even more true of the Kr* + N_2 and Ar* + N_2 reactions, where not even semiquantitative potentials have been developed. We just point out here that the superficial similarity of the trend of T_{rot} with v' in these two cases (increasing T_{rot} in going toward lower v') has to be qualified. For one, the dependence of T_{rot} on the exothermicity of a given product channel is much weaker for Kr* + N_2 than it is for Ar* + N_2. In the former case, the range spanned by the present experiment from $v' = 12$ to 5 represents an additional energy release of ~1.4 eV, and this is accompanied by a T_{rot} increase of only 200−350 K, depending on the collision energy. In contrast, for Ar* + N_2 the differential energy release between $N_2(C)$, $v' = 3$ and $v' = 0$ amounts to ~0.7 eV, but the corresponding T_{rot} increases by ~1800 K at 65 meV (Table 2). Furthermore, the description of the rotational distributions by the single parameter T_{rot} is too crude, at least for Ar* + N_2. Here several studies have shown that the J' distribution of the $N_2(C)$ product is actually bimodal.[2,11,12] For these reasons, the observed dependence of T_{rot} on v' may not be a reliable indicator of whether the Kr* + N_2 reaction does, in fact, involve an ionic intermediate.

Another useful criterion in this respect could be the energy dependence of the cross section, $Q(E_{CM})$. Figure 9, although semischematic, suggests that the crossing of the covalent entrance potential of Kr* + N_2 intersects the $Kr^+ + N_2$ curve at a point well above the asymptotic reactant energy. The reaction would then have a considerable activation energy (even taking into account that the barrier of the low adiabatic potential will lie a little below the crossing point of the diabatic curve, due to the “avoided” crossing). The cross section should then rise strongly with E_{CM}. If on the other hand the Kr* + N_2 reaction proceeds via the attractive branches V_{20} and V_{21} of the entrance potential, then no activation energy would be observed.

In the ionic case, the cross section would be small at the low collision energies used in this experiment, consistent with the weak signal observed (see above). At greater E_{CM}, Q should then rise noticeably. It was, in fact, found that the emission intensity was ~4.5 times greater at 191 meV than at 69 meV (which is the reason high-resolution spectra could only be taken at the highest energy, i.e., with the strongest seeding). However, this experimental “seed-gain factor” reflects only in part a possible increase of Q with E_{CM}. In addition, it is certainly also partly caused by an increasing concentration of the Kr* atoms on the beam axis. This density was not measured in the present work. In similar experiments with seeded Xe* beams, a seed gain of 10−15 was observed. In that case, the Xe* flux was measured by means of the secondary electron emission from a gold-plated surface, and it was found to increase ~12−14 times upon seeding. Thus the optically observed “seed gain” was mostly due to the increased Xe* flux. Since the Xe* velocity was only ~4 times greater with seeding, the Xe* number density in the beam must also have increased ~3-fold. Probably the discharge conditions with H_2 added to the Xe flow in the source gave a greater metastable Xe concentration. Similarly, the Kr* concentration in the present experiment may also have changed by H_2 seeding of the discharge, to an unknown extent. Therefore the question of whether the Kr* + N_2 reaction has an appreciable activation energy cannot be settled until reliable measurements of the relative Kr* flux at different seed conditions have been made.

VI. Conclusion

This work has yielded extensive, detailed experimental data on the collisional electronic energy transfer $Kr(^3P_2) + N_2(X) \rightarrow Kr(^1S_0) + N_2\ (B,v',J')$, which in the past has been little studied, since the luminescence from the $N_2(B)$ product is very weak. Comparing the results with those for the related systems $Xe(^3P_2) + N_2$ and $Ar(^3P_2) + N_2$, distinct parallels as well as dissimilarities have been found. Even so, a clear assignment of this reaction to either the ionic-intermediate (as Ar* + N_2) or the covalent type (as Xe* + N_2) has not been possible. More theoretical work is now called for, in particular calculations of the Kr* + N_2 potential that can accurately pinpoint the intersection with the Coulombic $Kr^+ + N_2^-(X)$ potential. On the other hand, experimental studies are needed to determine accurately the threshold behavior of the integral reaction cross section. This will necessitate the use of crossed beams and measurements of the relative Kr* flux as a function of energy.

We hope that the present high-resolution data will help to re-animate the studies of the important process of collisional electronic energy transfer in the comparatively simple three-atomic systems, which appears to have been somewhat neglected in recent years.

References and Notes

(1) Donovan, R. J.; Greenhill, P.; MacDonald, M. A.; Yencha, A. J.; Hartree, W. S.; Johnson, K.; Jouvet, C.; Kvaran, A.; Simons, J. P. *Faraday Discuss. Chem. Soc.* **1980**, *84*, 221.

(2) van Vliembergen, E. J. W.; Vredenbregt, E. J. D.; Kaashoek, G. H.; Jaspar, J. P. M. J.; van Lanen, M. M. M.; Janssens, M. F. M.; Verheijen, M. J.; Beijerinck, H. C. W. *Chem. Phys.* **1987**, *114*, 117.

(3) Vredenbregt, E. J. D.; Boom, W.; van Gerwen, R. J. F.; Beijerinck, H. C. W. *Chem. Phys.* **1990**, *145*, 267.

(4) Stedman, D. H.; Setser, D. W. *J. Chem. Phys.* **1970**, *52*, 3957.

(5) Tracy, C. J.; Oskam, H. J. *J. Chem. Phys.* **1976**, *65*, 1666.

(6) Sadeghi, N.; Setser, D. W. *Chem. Phys. Lett.* **1981**, *82*, 44.

(7) Tsuji, M.; Yamaguchi, K.; Nishimura, Y. *J. Chem. Phys.* **1988**, *89*, 3391.

(8) BelBruno, J.; Krenos, J. *Chem. Phys. Lett.* **1980**, *74*, 430.

(9) Krümpelmann, T.; Ottinger, Ch. *Chem. Phys. Lett.* **1987**, *140*, 142.

(10) Ottinger, Ch.; Vilesov, A. F.; Xu, D. D. *Chem. Phys.* **1995**, *192*, 49.

(11) Aquilanti, V.; Candori, R.; Pirani, F.; Krümpelmann, T.; Ottinger, Ch. *Chem. Phys.* **1990**, *142*, 47.

(12) Lishawa, C. R.; Allison, W.; Muschlitz, E. E., Jr. *J. Chem. Phys.* **1982**, *77*, 5855.

(13) Part I: Derouard, J.; Nguyen, T. D.; Sadeghi, N. *J. Chem. Phys.* **1980**, *72*, 6698. Part II: Nguyen, T. D.; Sadeghi, N. *Chem. Phys.* **1983**, *79*, 41.

(14) Geisen, H. Unpublished.

(15) Krümpelmann, T. Thesis Göttingen, Max-Planck-Institut für Strömungsforschung, Bericht 17, 1987.

(16) Abuaf, N.; Anderson, J. B.; Andres, R. P.; Fenn, J. B.; Miller, D. R. In *Rarefied Gas Dynamis*; Brundin, C. L., Ed.; Academic Press: New York, 1967; p 1317.

(17) Neuschäfer, D.; Ottinger, Ch.; Sharma, A. *Chem. Phys.* **1987**, *117*, 133.

(18) Müller, B. Thesis Göttingen, Max-Planck-Institut für Strömungsforschung, Bericht 18, 1988.

(19) Geisen, H. Thesis Göttingen, Max-Planck-Institut für Strömungsforschung, Bericht 3, 1989.

(20) Roux, F.; Michaud, F.; Verges, J. *J. Mol. Spectrosc.* **1983**, *97*, 253.

(21) Lefebvre-Brion, H.; Field, R. W. *Perturbations in the Spectra of Diatomic Molecules*; Academic Press: Orlando, FL, 1986.

(22) Geisen, H. Diplomarbeit, Max-Planck-Institut für Strömungsforschung, Göttingen, Bericht 113, 1988.

(23) Ehlich, R. Diplomarbeit, Max-Planck-Institut für Strömungsforschung, Göttingen, 1990.

(24) Werner, H.-J.; Kalcher, J.; Reinsch, E.-A. *J. Chem. Phys.* **1984**, *81*, 2420.

(25) Piper, L. G.; Holtzclaw, K. W.; Green, B. D.; Blumberg, W. A. M. *J. Chem. Phys.* **1989**, *90*, 5337.

(26) Eyler, E. E.; Pipkin, F. M. *J. Chem. Phys.* **1983**, *79*, 3654.

(27) Katayama, D. H. *J. Chem. Phys.* **1986**, *84*, 1477.

(28) Derouard, J.; Sadeghi, N. *Chem. Phys. Lett.* **1983**, *102*, 324.

(29) Steinfeld, J. J.; Klemperer, W. *J. Chem. Phys.* **1965**, *42*, 3475.

(30) Bergmann, K.; Demtröder, W. *J. Phys.* **1972**, *B5*, 2098.

(31) Ottinger, Ch. Méthodes de Spectroscopie sans Largeur Doppler de Niveaux Excités des Systèmes Moléculaires Simples. Coll. Intern. du CNRS No. 217, Aussois, 1973, p 49.

(32) Poppe, D. Thesis Göttingen. Max-Planck-Institut für Strömungsforschung, Bericht 103, 1974.

(33) Ottinger, Ch.; Schröder, M. *J. Phys.* **1980**, *B13*, 4163.

(34) Geisen, H.; Neuschäfer, D.; Ottinger, Ch. *J. Chem. Phys.* **1990**, *92*, 104.

(35) Krümpelmann, T.; Ottinger, Ch. *J. Chem. Phys.* **1988**, *88*, 5245.

(36) Chiu, L.-Y. C.; Chiu, Y.-N.; Krümpelmann, T.; Ottinger, Ch. *Chem. Phys. Lett.* **1988**, *151*, 220.

(37) Chiu, L.-Y. C.; Krümpelmann, T.; Ottinger, Ch. *Chem. Phys. Lett.* **1989**, *157*, 60.

(38) Böhle, W.; Geisen, H.; Krümpelmann, T.; Ottinger, Ch. *Chem. Phys.* **1989**, *133*, 313.

(39) Weissmann, G.; Ganz, J.; Siegel, A.; Waibel, H.; Hotop, H. *Opt. Commun.* **1984**, *49*, 335.

(40) Sobczynski, R.; Beaman, R.; Setser, D. W.; Sadeghi, N. *Chem. Phys. Lett.* **1989**, *154*, 349.

(41) Sobczynski, R.; Setser, D. W. *J. Chem. Phys.* **1991**, *95*, 3310.

(42) Cerny, D.; Roux, F.; Effantin, C.; d'Incan, J. *J. Mol. Spectrosc.* **1980**, *81*, 216.

(43) Nyeland, C.; Toennies, J. P. *Chem. Phys. Lett.* **1986**, *127*, 172.

(44) Huber, K. P.; Herzberg, G. *Constants of Diatomic Molecules*; Molecular Spectra and Molecular Structure, Vol. 4; Van Nostrand: Princeton, NJ, 1979.

(45) Radzig, A. A.; Smirnov, B. M. *Reference Data on Atoms, Molecules and Ions*; Toennies, J. P., Ed.; Springer: Berlin, 1985.

(46) Aquilanti, V.; Candori, R.; Pirani, F.; Ottinger, Ch. *Chem. Phys.* **1994**, *187*, 171.